Dopant Concentration - Porosity - Li-ion Conductivity Relationship in Garnet-Type $Li_{5+2x}La_3Ta_{2-x}Y_xO_{12}$ ($0.05 \leq x \leq 0.75$) and Their Stability in Water and 1M LiCl

Sumaletha Narayanan, Farshid Ramezanipour, and Venkataraman Thangadurai*

Department of Chemistry, University of Calgary, 2500 University Dr NW, Calgary, AB, Canada T2N 1N4, *vthangad@ucalgary.ca Phone 1 (403) 210 8649

Abstract. Highly Li-ion conductive Y-doped garnet-type $Li_{5+2x}La_3Ta_{2-x}Y_xO_{12}$ ($0.05 \leq x \leq 0.75$) were studied to understand the effects of yttrium and lithium-doping on chemical composition, crystal structure, porosity and Li-ion conductivity using ^{7}Li MAS NMR, electrochemical AC impedance spectroscopy and scanning electron microscopy (SEM), as well as ex-situ and in-situ powder X-ray diffraction (PXRD) to further explore the potential application of garnets in all-solid-state Li ion batteries. Solid-state ^{7}Li MAS NMR studies showed an increase in the Li ion mobility as a function of Y and Li-doping in $Li_{5+2x}La_3Ta_{2-x}Y_xO_{12}$, which is consistent with the results from ac impedance spectroscopy. The SEM studies on sintered pellets indicated a systematic decrease in porosity and increase in sinterability as the Y and Li-doping level increases in $Li_{5+2x}La_3Ta_{2-x}Y_xO_{12}$. These results are consistent with the calculated porosity and densities using the Archimedes method. Using the variable temperature in-situ PXRD, a thermal expansion coefficient of 7.25 x 10^{-6} K^{-1} was observed for $Li_6La_3Ta_{1,5}Y_{0.5}O_{12}$ in the temperature range of 30- 700 °C. To further explore the possibility of a new application for the Li-stuffed garnets, the stability of these materials in aqueous LiCl solution was also studied. A high degree of structural stability was observed in these materials upon 1M LiCl treatment, making them suitable candidates for further studies as protective layers for lithium electrodes in aqueous lithium batteries.

1. INTRODUCTION

The study of lithium ion conductivity in solid-state materials is motivated by the development of all-solid-state batteries, where the liquid electrolytes are replaced by Li ion conducting solid electrolytes, which can lead to improved safety, stability and energy density. Recently, the garnet-type Li-stuffed metal oxides have shown excellent potential for application as solid Li ion electrolytes.[1] Several members of the garnet family have shown high Li ion conductivity, chemical stability to elemental Li and large electrochemical window at room temperature.[2] In addition to solid electrolyte applications, another area where Li ion conducting solids can be exploited is in lithium-air batteries. Aqueous electrolytes in these batteries need to be separated from the elemental lithium anode to prevent the vigorous reaction of lithium with water. To protect the lithium electrode, protective layers consisting of Li ion conducting solids that are stable in contact with water and elemental Li are desired.[3-5]

The first reported Li ion conducting garnets, $Li_5La_3M_2O_{12}$ (M = Nb, Ta), showed total Li conductivity (bulk + grain-boundary) of 10^{-6} Scm^{-1} at room temperature.[6] The Ta analogue showed better chemical reaction stability toward molten Li metal and a wider voltage window (> 6V) compared to the Nb member.[7] The Li ion conductivity can be significantly improved by partial substitution at La or M sites.[8-11] Murugan et al. have synthesized (~ 1230 °C) cubic $Li_7La_3Zr_2O_{12}$ garnet with a conductivity of ~ 10^{-4} Scm^{-1} at room temperature, which shows good stability towards metallic Li, and therefore, it has been widely studied for all-solid-state Li ion batteries.[12] However, $Li_7La_3Zr_2O_{12}$ crystallizes in tetragonal geometry when the synthesis temperature is lowered to 980 °C, which possesses 2 orders of magnitude lower conductivity than the cubic phase.[13] Hence, it is important to stabilize the cubic phase of garnets to achieve promising Li ion conductivity, and dopants such as Al, Ta, Nb, and Y have proven to help to achieve this goal.[14-22] Rangasamy et al. studied the effect of both Li and Al on $Li_7La_3Zr_2O_{12}$ structure and optimized the amount of Al (0.204 mol.) to stabilize the cubic

phase.[16] Substitution of Y, Nb and Ta led to the improvement of the bulk conductivity of $Li_7La_3Zr_2O_{12}$ from ~ 10^{-4} to ~ 10^{-3} Scm^{-1} at room temperature.[20, 22, 23] Also, stabilization of cubic phase at lower temperature (1000 °C) was observed upon Ta substitution at Zr-site in $Li_7La_3Zr_2O_{12}$.[19]

Recently, we showed that the ionic conductivity of $Li_5La_3Nb_2O_{12}$ can be enhanced by partial doping of Y at the Nb-sites, leading to the Li-conductivity of up to 10^{-4} Scm^{-1} at room temperature.[24] Given the wider voltage window and higher stability of the Ta analogue, $Li_5La_3Ta_2O_{12}$, to metallic lithium, we envisioned the possibility of obtaining high ionic conductivity in the Ta compounds, where both high stability and Li conductivity can be present. Subsequently, we synthesized and studied the low temperature dielectric properties of the Y-doped $Li_{5+2x}La_3Ta_{2-x}Y_xO_{12}$ (x = 0.25, 0.5 and 0.75).[25] We showed that the x = 0.5 and 0.75 phases show high conductivity at room temperature, in the order of 10^{-4} Scm^{-1}.[25] Here, we present the detailed study of Y-doped $Li_5La_3Ta_2O_{12}$ phases in a wide temperature range, the trend in their porosity, sinterability and Li ion conductivity using ^7Li MAS NMR, ac impedance spectroscopy, scanning electron microscopy, and porosity/density measurements. In addition, we show the stability of these materials in aqueous LiCl (1M) solution, making them potential candidates for application as protective layers for lithium electrodes in lithium aqueous batteries.[3-5]

2. EXPERIMENTAL

2.1 Sample preparation of $Li_{5+2x}La_3Ta_{2-x}Y_xO_{12}$ ($0.05 \leq x \leq 0.75$). The syntheses were performed according to a procedure reported elsewhere.[25] Specifically, desired amounts of $LiNO_3$ (99%, Alfa Aesar), La_2O_3 (99.99%, Alfa Aesar) (preheated at 900 °C for 24h), Ta_2O_5 (99.5%, Alfa Aesar), and $Y(NO_3)_3$ (99.9%, Alfa Aesar) were thoroughly mixed by ball-milling using 2-propanol, and then were heated at 700 °C. After the heat treatment, the powder mixture was ball-milled again and pressed into pellets using an isostatic press. The pellets were covered with mother powder in an alumina crucible and

were initially heated to 900 °C for 24 h followed by a final sintering at 1100 °C for 6 h to ensure the garnet-phase formation.

2.2 Structural and electrical analyses of $Li_{5+2x}La_3Ta_{2-x}Y_xO_{12}$ ($0.05 \leq x \leq 0.75$). The phase analysis was done using powder X-ray diffraction (PXRD) data obtained on a Bruker D8 powder X-ray diffractometer with Cu Kα radiation. Solid-state ^{27}Al and ^{7}Li magic angle spinning nuclear magnetic resonance (MAS NMR) studies were performed using (AMS 300, Bruker, at a spinning rate 5 kHz) against solid $Al(NO_3)_3$ and LiCl as standards. The morphological studies were carried out using scanning electron microscopy (SEM) (Philips FEI XL30). The pellets were cut into small discs using a diamond saw for the SEM analysis. Archimedes method was used to measure the density of garnets in pellet form using methanol. The ac impedance spectroscopy on the pellets using Au electrodes was carried out on a Solartron SI 1260 impedance and gain-phase analyzer (0.01 Hz to 1 MHz; 100 mV) in ambient atmosphere.

2.3 Chemical stability of $Li_{5+2x}La_3Ta_{2-x}Y_xO_{12}$ ($0.05 \leq x \leq 0.75$) with respect to temperature, water and LiCl. Thermal stability test was conducted using thermo gravimetric analysis (TGA) (Mettler Toledo thermal system; TGA/DSC1 HT 1600 °C system) in the range of 25-800°C under N_2 atmosphere at a ramping rate of 10 °C/min. The structural stability of as-prepared $Li_{5+2x}La_3Ta_{2-x}Y_xO_{12}$ at different temperatures was studied by variable temperature in-situ PXRD using a high temperature chamber (Anton Paar XRK 900) on the same diffractometer mentioned above. In order to analyze the chemical stability of $Li_{5+2x}La_3Ta_{2-x}Y_xO_{12}$ in water, the powder was stirred in water for 2 days. The stability in aqueous LiCl solution was determined by stirring pellets of $Li_{5+2x}La_3Ta_{2-x}Y_xO_{12}$ in 1 M LiCl for 1 week, after which the pellets were vacuum dried at ~ 100 °C for 6 h prior to the PXRD and conductivity measurements.

3. RESULTS AND DISCUSSION

3.1 Phase analysis of $Li_{5+2x}La_3Ta_{2-x}Y_xO_{12}$. Rietveld refinements[26, 27] with powder X-ray diffraction data were performed to confirm the formation of the garnet-type structure in $Li_{5+2x}La_3Ta_{2-x}Y_xO_{12}$ phases. The results of these analyses for the x = 0.05, 0.1 and 0.2 phases are shown in Table 1, and a typical Rietveld refinement profile, in this case for x = 0.2 member, is presented in Figure 1. We have recently reported the structural parameters for the x = 0.25, 0.5 and 0.75,[25] and hence, these members will not be presented in this work. For all $Li_{5+2x}La_3Ta_{2-x}Y_xO_{12}$ ($0.05 \leq x \leq 0.75$) phases a cubic structure with space group *Ia*-3*d* can be identified. Due to the larger ionic radius of Y^{3+} (0.90 Å) compared to Ta^{5+} (0.64 Å),[28] an increase in the unit cell dimension is expected as the amount of Y^{3+} increases in $Li_{5+2x}La_3Ta_{2-x}Y_xO_{12}$. This increase can be observed from the data shown in Table 1. In the garnet-type structure, the transition metals (Ta or Y) are octahedrally coordinated by oxygen atom (Figure 2a). The $Ta(Y)O_6$ octahedra are not connected to each other and do not share corners or edges, unlike in the perovskite-type structure.[29] The La and Li atoms reside in the spaces in between these octahedra. The coordination sphere of La consists of eight oxygen atoms, forming dodecahedral geometry with triangular faces around the La atom (Figure 2d).

The Li ions sites in Li-stuffed garnets are well established in the literature,[10, 14,25, 30-32] but given the essential role of Li distribution in Li-ion conductivity, some remarks are given in this work. Three crystallographically distinct Li positions are known for this structure type.[30, 31] Li(1) is located at the center of a tetrahedron formed by oxygen atoms (24d site in Figure 3a), while Li(2) is at the center of an octahedron (48g site). Some of the Li atoms are shifted from the centers of the 48g site octahedra, leading to a new crystallographic positions, 96h, for Li(3). Note that the octahedra are connected to the tetrahedra through face-sharing. There is also edge-sharing between neighboring octahedra, as seen in Figure 3. The above arrangement leads to an array of Li atoms surrounded by octahedral or tetrahedral

geometry, which form a three-dimensional network throughout the material (Figure 3b), leading to the high Li-ion conductivity observed in these systems. It is important to note that all of the sites shown in Figure 3 cannot be occupied simultaneously due to short Li – Li contacts.[24] An octahedral site will remain vacant if both tetrahedral sites adjacent to it are occupied.[31, 32] While the occupancy of Li positions cannot be determined by laboratory PXRD, it is possible to obtain an estimate of the Li occupancy on each site based on the neutron diffraction data on similar materials. O'Callaghan and Cussen have studied $Li_{5+x}Ba_xLa_{3-x}Ta_2O_{12}$ (x = 0, 0.5, 1, 1.2, 1.4, 1.6) and have shown a correlation between the total Li-content in the system and the occupancy of Li on each of the three sites, 24*d*, 48*g* and 96*h*.[31] Based on their neutron diffraction data, there is an increase in the Li occupancy on the octahedral sites, 48*g* and especially 96*h*, as a function of total Li-content. On the other hand, the Li occupancy on the 24*d* site (centers of tetrahedra) decreases as the total Li-content increases in Li-stuffed garnets.[1,2] The above information was used to estimate the Li occupancy on each site in our $Li_{5+2x}La_3Ta_{2-x}Y_xO_{12}$ phases, as shown in Table 1. A mechanism for Li conduction has also been proposed before,[20, 25] which relies primarily on the Li-hopping between the octahedral sites, implying that greater Li-mobility should be associated with higher octahedral site occupancy.

3.2 Li ion conductivity as a function of Y-doping and temperature. The remarkable room temperature conductivity of the x = 0.5 and 0.75 phases of $Li_{5+2x}La_3Ta_{2-x}Y_xO_{12}$, ~$10^{-4}$ Scm^{-1},[25] prompted us to study the conductivity over a much wider temperature range of 23 to 325 °C, and look at the conductivity trends as a function of doping and temperature for the entire series from x = 0.05 to x = 0.75. In addition, we show the dependence of the Li ion mobility on Li-content using ^{7}Li MAS NMR spectroscopy. Typical AC-impedance data of $Li_{5+2x}La_3Ta_{2-x}Y_xO_{12}$ (x = 0.05-0.5) recorded at room temperature are shown in Figure 4 and they show one or two semicircle at the high-frequency side and a spike at the low-frequency side. This behavior is typical for Li-stuffed garnet-type structure solid Li ion

electrolytes.[6, 7, 33] The data is fitted using an equivalent circuit of resistances and constant phase elements (CPEs) and is shown as inset in Figure 4. The open symbols and the solid lines represent the measured and fitted data, respectively. The equivalent circuits represent the contributions from the electrical bulk, grain-boundary and electrode responses. The capacitance (C) value is calculated according to the equation 1.

$$C = R^{\left(\frac{1-n}{n}\right)} CPE^{\left(\frac{1}{n}\right)} \qquad (1)$$

where *R, CPE,* and *n* represent the resistance, constant phase element and fitting parameter. The lower doped $Li_{5+2x}La_3Ta_{2-x}Y_xO_{12}$ (x = 0.05 and 0.10) were fitted using the equivalent circuits comprising two sets of parallel R and CPE components and a series CPE component compared to the higher doped $Li_{5+2x}La_3Ta_{2-x}Y_xO_{12}$ (x = 0.20-0.5) where only one set of R and CPE parallel circuit was used. The calculated bulk and grain-boundary capacitance are in the range of 10^{-11} – 10^{-12} and 10^{-8} F, respectively which are in agreement with values expected for these materials (Table 2 and 3).[34] The goodness of fit is indicated by χ^2, where lower χ^2 indicates greater reliability of the fit. In all cases very low χ^2 values, in the order of 10^{-4}, were obtained, indicating excellent fits.

The results of the electrical conductivity studies at the temperature range of 23 to 325 °C are given in the Arrhenius plots (Figure 5a). As the temperature increases, the total (bulk + grain-boundary) conductivity increases as expected for garnet-type materials. In addition, the conductivity increases with increase in Li content and Y-doping, confirming once again that Li stuffing helps to increase the ionic conductivity in garnets.[24, 35] A decrease in activation energy from 0.43 to 0.33 eV (calculated at 23-325 °C) was observed with the increase in x in $Li_{5+2x}La_3Ta_{2-x}Y_xO_{12}$, as shown in Table 4 along with the total conductivity values at 23 °C. Note that activation energies from the data at a wide temperature range (23-325 °C) are generally smaller than those reported before for the x = 0.25, 0.5 and 0.75 using the low temperature data from -50 to 50 °C.[25]

The conductivity trend as a function of Li-content is also consistent with the results of the ^{7}Li magic angle spinning NMR studies. Figure 6a shows the ^{7}Li MAS NMR data, which are expressed against the chemical shift value of solid LiCl. A characteristic single peak near 0 ppm is observed and is the typical behavior of garnet-type compounds.[36, 37] As the Y-doping and the Li content increase, the peak becomes narrower, indicating faster mobility of Li, and confirming that the Li ion mobility is enhanced as a function of lithium content in the materials.

In addition, we were interested in verifying if our materials contain any Al, because there have been reports of the inclusion of Al from the alumina crucible into another garnet $Li_7La_3Zr_2O_{12}$, during sintering, which appeared to stabilize the cubic structure versus tetragonal in that material.[14, 17] Therefore, ^{27}Al magic angle spinning (MAS) NMR measurements were performed on all samples and indicated the presence of Al in $Li_{5+2x}La_3Ta_{2-x}Y_xO_{12}$ ($0.05 \leq x \leq 0.75$). As seen in Figure 6b, these are two peaks in the ^{27}Al MAS NMR data. The peak appearing in the range of 10-15 ppm, represents octahedrally coordinated Al, and has been proposed previously to correspond to small amounts of $LaAlO_3$.[8] However, recently it has been shown that Al originating from the alumina crucible can be included in the garnet structure by residing on the octahedral 48*g* site and sharing that site with lithium.[15] The ^{27}Al MAS NMR peaks appearing in the range of 70-80 ppm, correspond to Al in 4-fold coordination based on the chemical shift.[8] It has been suggested previously that these four-coordinated Al atoms are located in some of the 24*d* tetrahedral sites in the garnet structure, sharing that site with lithium.[14, 17] Therefore, the ^{27}Al MAS NMR data indicate the inclusion of trace amounts of aluminum in our materials. However, it is unclear if this Al inclusion plays any role in the stabilization of the cubic structure in the investigated garnet phases.

3.3 Trends in porosity and sinterabiliy as a function of Y-doping. Using scanning electron microscopy (SEM) and porosity/density calculations, a correlation has been established between the Y

(and Li) content and the sinterability of $Li_{5+2x}La_3Ta_{2-x}Y_xO_{12}$ ($0.05 \leq x \leq 0.75$). The scanning electron micrographs for $Li_{5+2x}La_3Ta_{2-x}Y_xO_{12}$ are shown in Figure 7. As seen here, a high degree of porosity is present in the sintered pellets of materials that have smaller degree of doping, while the pellets become considerably denser upon increasing the Y (and Li) content. The SEM results are also qualitatively consistent with the percent-porosity values (Table 5) obtained based on Archimedes principle. The porosity of the samples can be calculated using the formula:[38]

$$\%\,porosity = \left(\frac{W_{Sat} - W_{Dry}}{W_{Sat} - W_{Susp}} \right) \text{x}100 \qquad (2)$$

where W_{Sat}, W_{Dry} and W_{Sus} indicate the saturated, dry and suspended weights, respectively. The porosities of sintered pellets for x = 0.05, 0.1, 0.2 and 0.25 are close to each other and range between 28 – 35 %. However, there is a significant decrease in porosity for x = 0.5 and 0.75, where the calculated porosities are about 0.5 % and 1.6 %, respectively. These results are found to be consistent with the densities of sintered pellet (Table 5) obtained using the Archimedes method based on equation 3.

$$D_{Archimedes} = \frac{W_{Dry}}{\left(\frac{W_{Sat} - W_{Susp}}{0.7918} \right)} \qquad (3)$$

The constant 0.7918 in equation 3 is the room temperature density of methanol (g/cm^3) that was used as the suspension medium in the Archimedes technique. Methanol was used instead of water because garnets tend to exchange Li ions with water that can affect the accuracy of the density measurements. The potential exchange of Li in methanol has not been considered. The theoretical density (d) was computed from the PXRD data using the expression,

$$d = \frac{ZM}{a^3 N_A} \qquad (4)$$

where Z is the number of chemical formula per unit cell (Z = 8), M is the molar weight of the nominal chemical composition $Li_{5+2x}La_3Ta_{2-x}Y_xO_{12}$, '*a*' is the lattice parameter obtained from PXRD, and N_A is Avogadro's number. As shown in Table 5, the densities of the x = 0.5 and 0.75 are significantly greater than the densities obtained for x = 0.05, 0.1, 0.2 and 0.25, again confirming the direct correlation between the doping level and sinterability in these materials.

3.4 Structural stability and chemical compatibility with aqueous LiCl solution. The high structural stability of $Li_{5+2x}La_3Ta_{2-x}Y_xO_{12}$ was studied by in-situ PXRD in the temperature range of 30-700 °C as shown in Figure 8. The thermal expansion coefficient (TEC) of $Li_{5+2x}La_3Ta_{2-x}Y_xO_{12}$ (x = 0.5) with temperature was calculated using the lattice parameters derived from in-situ PXRD (Figure 8b). The formula used for TEC calculation is shown in equation 5:

$$\alpha = \left(\frac{a - a_0}{a_0} \right) \left(\frac{1}{T - T_0} \right) \qquad (5)$$

where α, T and a represent the thermal expansion coefficient, temperature, and lattice parameter at that temperature.[39] The notations a_0, and T_0 represent the corresponding values at room temperature. A thermal expansion coefficient of 7.25 x 10^{-6} K^{-1} was observed for $Li_6La_3Ta_{1,5}Y_{0.5}O_{12}$.

To determine the stability in aqueous environments, the materials were treated in water as described in the experimental section. The water-treated materials were then studied by variable temperature PXRD to determine if there were any changes in their structure or stability. Figure 9 shows the corresponding data for the x = 0.5 phase and indicates that the water-treated material maintains the cubic structure and is also structurally stable up to 700 °C. We next explored the potential application of $Li_{5+2x}La_3Ta_{2-x}Y_xO_{12}$ as protective layer for the lithium anode in Li aqueous batteries, where a highly Li-conductive material that has chemical compatibility with aqueous lithium salts, is desired. Therefore, compatibility tests with 1 M aqueous LiCl solution were performed as described in the experimental

section. The pH change was monitored for one week and result is shown in Figure 10. The change in pH indicates the potential exchange of Li^+ with proton in $Li_{5+2x}La_3Ta_{2-x}Y_xO_{12}$. An increase in the pH value was observed over the first 2 days, reaching a maximum value of 11-11.5 from initial value of 6, and remained almost constant for the rest of the week. Similar change in pH as reported in other garnets in water.[40, 41] A comparative impedance study of the aqueous LiCl-treated garnets was also performed.

Figure 11 shows the ac impedance plots of LiCl treated $Li_{5+2x}La_3Ta_{2-x}Y_xO_{12}$ (x = 0.50 and 0.75) measured at 75 °C. The grain-boundary impedance was found to be increasing after the aqueous LiCl treatment in all the cases. As shown in the Arrhenius plot (Figure 5b), the conductivity also drops compared to the as-prepared garnets. This may be partly due to the replacement of Li^+ in the garnet structure with H^+ from the aqueous solution. The pH change during the aqueous LiCl treatment and the presence of –OH peaks in the FTIR spectra (~ 3500 cm^{-1} for –OH stretching and ~ 1500 cm^{-1} for –OH bending) shown in Figure 12 indicate that there was an ion exchange between the garnet and water during the water treatment.

In order to understand the microstructure, a cross sectional SEM imaging was also done on the pellets treated in aqueous LiCl as shown in Figure 13. The SEM data indicated a greater degree of porosity in the samples after aqueous LiCl treatment compared to the untreated materials (Figure 7). The EDX patterns were recorded (Figure 13) in search for chlorine to examine the potential entrapment of LiCl in the pores. However, no evidence was found to indicate the presence of significant amount of chlorine in these samples (Figure 13). Nevertheless, note that even after the drop in conductivity, the measured values are still significantly greater than the conductivity of the parent un-doped compound.[6] The PXRD data of the samples treated after the aqueous LiCl test shows that there is no phase change indicating high structural stability of the garnets as shown in Figure 14. Thus, the garnet-type

$Li_{5+2x}La_3Ta_{2-x}Y_xO_{12}$ materials show a high stability under aqueous LiCl environment making them suitable candidates for potential application in Li aqueous batteries.

4. CONCLUSIONS

The garnet-type $Li_{5+2x}La_3Ta_{2-x}Y_xO_{12}$ ($0.05 \leq x \leq 0.75$) was deeply studied to correlate the Y and Li content with conductivity, porosity and sinterability. ^{7}Li magic angle spinning NMR shows a direct correlation between the Li-content and lithium mobility in these materials, which is consistent with the impedance spectroscopy studies that indicate higher conductivity for materials with greater Li-content. The conductivity of these materials over a wide temperature range, from 23 °C to 325 °C, has also been studied. In addition, with the aid of scanning electron microcopy and Archimedes calculations of porosity and density, a correlation has been established between the sinterability and dopant content, where an increase in sinterability is observed as the Li (and Y) contents increase. Furthermore, stability tests were performed to determine the compatibility of these materials with aqueous LiCl, indicating some decrease in Li-conductivity but very high stability, making $Li_{5+2x}La_3Ta_{2-x}Y_xO_{12}$ a potential candidate for further investigation as protective layer for lithium electrodes in lithium-air batteries.

AUTHOR CONTACT INFORMATION

Corresponding Author

E-mail: vthangad@ucalgary.ca; Phone: 1 (403) 210 8649. Fax: 1 (403) 289 9488.

Notes

The authors declare no competing financial interest.

ACKNOWLEDGEMENTS

One of the authors (V.T.) would like to thank the Natural Sciences and Engineering Research Council of Canada (NSERC) Discovery Grants (DG) program.

Table 1. The Rietveld refinement results for $Li_{5+2x}La_3Ta_{2-x}Y_xO_{12}$ (x = 0.05 - 0.20). The Li occupancies are based on the values in reference 4.

	x = 0.05	**x = 0.10**	**x = 0.20**
La (24*c*) occupancy	1	1	1
x	1/8	1/8	1/8
y	0	0	0
z	1/4	1/4	1/4
U_{iso}	0.0230(8)	0.0209(7)	0.0224(7)
Ta/Y (16*a*) occupancy	0.975/0.025	0.95/0.05	0.90/0.10
x	0	0	0
y	0	0	0
z	0	0	0
U_{iso}	0.0214(7)	0.0198(6)	0.0206(6)
Li1 (24*d*) occupancy	0.768	0.7453	0.705
x	1/4	1/4	1/4
y	7/8	7/8	7/8
z	0	0	0
U_{iso}	0.025	0.025	0.025
Li2 (48*g*) occupancy	0.156	0.174	0.207
x	1/8	1/8	1/8
y	0.6826	0.6826	0.6826
z	0.5674	0.5674	0.5674
U_{iso}	0.025	0.025	0.025
Li3 (96*h*) occupancy	0.155	0.16	0.1702
x	0.0927	0.0927	0.0927
y	0.684	0.684	0.684
z	0.5795	0.5795	0.5795
U_{iso}	0.025	0.025	0.025
O (96*h*) occupancy	1	1	1
x	0.2896(6)	0.2883(5)	0.2868(5)
y	0.0990(6)	0.1012(5)	0.1012(5)
z	0.19846)	0.1984(6)	0.1996(6)
U_{iso}	0.0207(31)	0.0212(29)	0.0215(28)
R_p (%)	9.18	8.58	8.25
R_{wp} (%)	11.83	11.17	11.01
a (Å)	12.8160(3)	12.8268(4)	12.8642(3)

Table 2. AC impedance fitting results of $Li_{5+2x}La_3Ta_{2-x}Y_xO_{12}$ (x = 0.05 and 0.10).

x	R_b (Ω)	CPE_b (F)	C_b (F)	R_{gb} (Ω)	CPE_{gb} (F)	C_{gb} (F)	CPE_{el} (F)	χ^2
0.05	1.69×10^{4}	5.70×10^{-10}	1.37×10^{-11}	2.18×10^{4}	1.59×10^{-7}	2.07×10^{-8}	3.33×10^{-6}	0.0002
0.10	1.49×10^{4}	1.40×10^{-9}	1.55×10^{-11}	4.84×10^{4}	3.34×10^{-8}	1.32×10^{-8}	9.05×10^{-7}	0.0003

Table 3. The room temperature AC impedance fitting results of $Li_{5+2x}La_3Ta_{2-x}Y_xO_{12}$ (x = 0.20, 0.25, and 0.50).

x	R_b (Ω)	CPE_b (F)	C_b (F)	CPE_{el} (F)	χ^2
0.20	2.00×10^{4}	2.83×10^{-9}	1.12×10^{-11}	6.74×10^{-6}	0.0008
0.25	8.89×10^{4}	1.77×10^{-9}	8.06×10^{-12}	3.24×10^{-6}	0.0008
0.50	2.26×10^{4}	8.48×10^{-9}	2.10×10^{-12}	3.00×10^{-6}	0.0001

Table 4. The room temperature (25 °C) conductivity and activation energies of $Li_{5+2x}La_3Ta_{2-x}Y_xO_{12}$ calculated at 23-325 °C. We have reported the conductivity values for x = 0.25, 0.5 and 0.75 before.[25] These values are repeated here to show the trend.

x in $Li_{5+2x}La_3Ta_{2-x}Y_xO_{12}$	$\sigma_{23\,°C}$ (Scm^{-1})	E_a (eV)
0.05	9.56×10^{-6}	0.43
0.10	1.04×10^{-5}	0.40
0.20	1.07×10^{-5}	0.44
0.25	2.82×10^{-5}	0.43
0.50	1.26×10^{-4}	0.37
0.75	1.83×10^{-4}	0.33

Table 5. Calculated and measured density results of $Li_{5+2x}La_3Ta_{2-x}Y_xO_{12}$ from PXRD and Archimedes methods.

x in $Li_{5+2x}La_3Ta_{2-x}Y_xO_{12}$	Measured Density (gcm^{-3})	Theoretical Density (gcm^{-3})	Archimedes Porosity (%)
0.05	3.463	6.320	29
0.10	3.114	6.279	35
0.20	3.353	6.176	30
0.25	3.479	6.104	28
0.50	4.919	5.928	0.5
0.75	4.776	5.772	1.6

Figure Captions

Figure 1. Rietveld refinement profile for $Li_{5.24}La_3Ta_{1.8}Y_{0.2}O_{12}$, indicating the formation of garnet-type structure.

Figure 2. The garnet-type structure of $Li_{5+2x}La_3Ta_{2-x}Y_xO_{12}$ **(a)** Ta-O sublattice. Ta is shown in blue and oxygen in red. **(b)** Ta-O sublattice with La (purple) in spaces between TaO_6 units. **(c)** TaO_6 units shown by grey octahedra. La atoms are in purple, while Li1 (24d site) and Li2 (48g site) are shown as blue and green spheres, respectively. Li3 (96h site) is omitted for clarity. **(d)** The La-O sublattice showing LaO_8 polyhedra.

Figure 3. (a) The tetrahedral and octahedral arrangements of oxygens that accommodate the Li atoms. Oxygens are shown as small red spheres at the corners of polyhedra. The Li atoms at the centers of tetrahedra (24d site) and octahedra (48g site) are shown in blue and light green, respectively. The Li atom that is shifted from the center of the octahedron (96h site) is shown in dark green. **(b)** Three-dimensional connectivity of oxygen octahedra and tetrahedra, which can accommodate Li atoms, shown as blue and green spheres. In the actual structure, not all of the neighboring sites can be simultaneously occupied by Li and it is not possible for a Li atom to exist at an octahedral site if both tetrahedral sites adjacent to it are occupied.

Figure 4. Typical AC impedance plots at 23 °C for $Li_{5+2x}La_3Ta_{2-x}Y_xO_{12}$ ($0.05 \leq x \leq 0.5$) (a) x = 0.05, (b) x = 0.10, (c) x = 0.20, (d) x = 0.25, and (e) x = 0.50. The open symbols represent the collected data and the solid lines represent the fitting. The inset figure indicates the equivalent circuits used for fitting analysis.

Figure 5. Arrhenius plots showing the conductivity variation against temperature of a) as-prepared $Li_{5+2x}La_3Ta_{2-x}Y_xO_{12}$ ($0.05 \leq x \leq 0.75$) and b) $Li_{5+2x}La_3Ta_{2-x}Y_xO_{12}$ (x = 0.5, and 0.75) after treatment with 1 M LiCl solution.

Figure 6. (a) ^{7}Li and (b) ^{27}Al MAS NMR of $Li_{5+2x}La_3Ta_{2-x}Y_xO_{12}$ ($0.05 \leq x \leq 0.75$). Chemical shift was measured against solid LiCl for Li MAS, and $Al(NO_3)_3$ for Al MAS NMR. A spinning frequency of 5 kHz was used.

Figure 7. Morphological studies of $Li_{5+2x}La_3Ta_{2-x}Y_xO_{12}$ (x = 0.05–0.75) pellets using SEM microscopy.

Figure 8. In situ PXRD of $Li_{5+2x}La_3Ta_{2-x}Y_xO_{12}$ (a) x = 0.25 and (b) x = 0.5 showing the thermal stability.

Figure 9. In situ PXRD patterns of water treated $Li_6La_3Ta_{1,5}Y_{0.5}O_{12}$ showing the structural stability.

Figure 10. Changes in the pH during the treatment of $Li_{5+2x}La_3Ta_{2-x}Y_xO_{12}$ (x = 0.50 and 0.75) in 1 M LiCl solution.

Figure 11. Impedance spectra of $Li_{5+2x}La_3Ta_{2-x}Y_xO_{12}$ (x = 0.50 and 0.75) after treatment with 1 M LiCl solution measured at 75 °C. The inset magnifies the data for x = 0.50 sample to show the small semi-circle at the high frequency side.

Figure 12. FTIR spectra of water-treated $Li_{5+2x}La_3Ta_{2-x}Y_xO_{12}$ (x = 0.25, 0.5 and 0.75).

Figure 13. SEM images and EDX results for $Li_{5+2x}La_3Ta_{2-x}Y_xO_{12}$ (x = 0.5 and 0.75) after treatment with 1 M LiCl solution.

Figure 14. PXRD of $Li_{5+2x}La_3Ta_{2-x}Y_xO_{12}$ (x = 0.5 and 0.75) after reaction with 1 M LiCl solution.

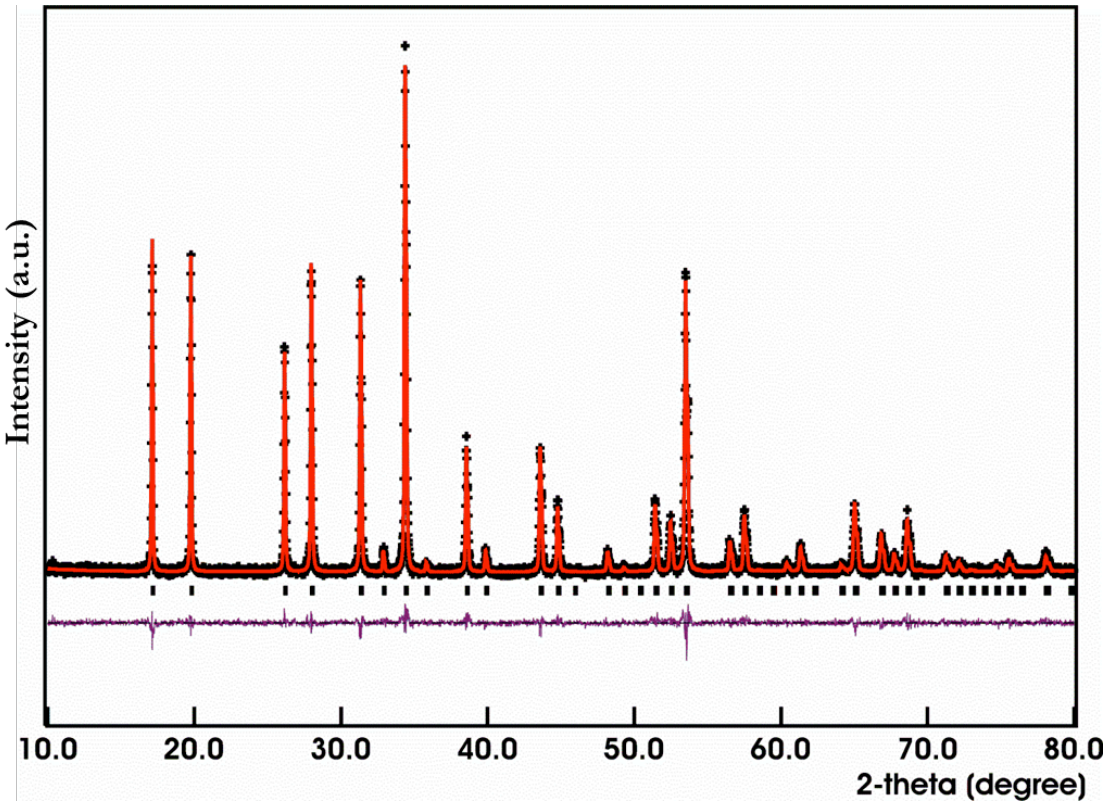

Figure 1. Rietveld refinement profile for $Li_{5.24}La_3Ta_{1.8}Y_{0.2}O_{12}$, indicating the formation of garnet-type structure.

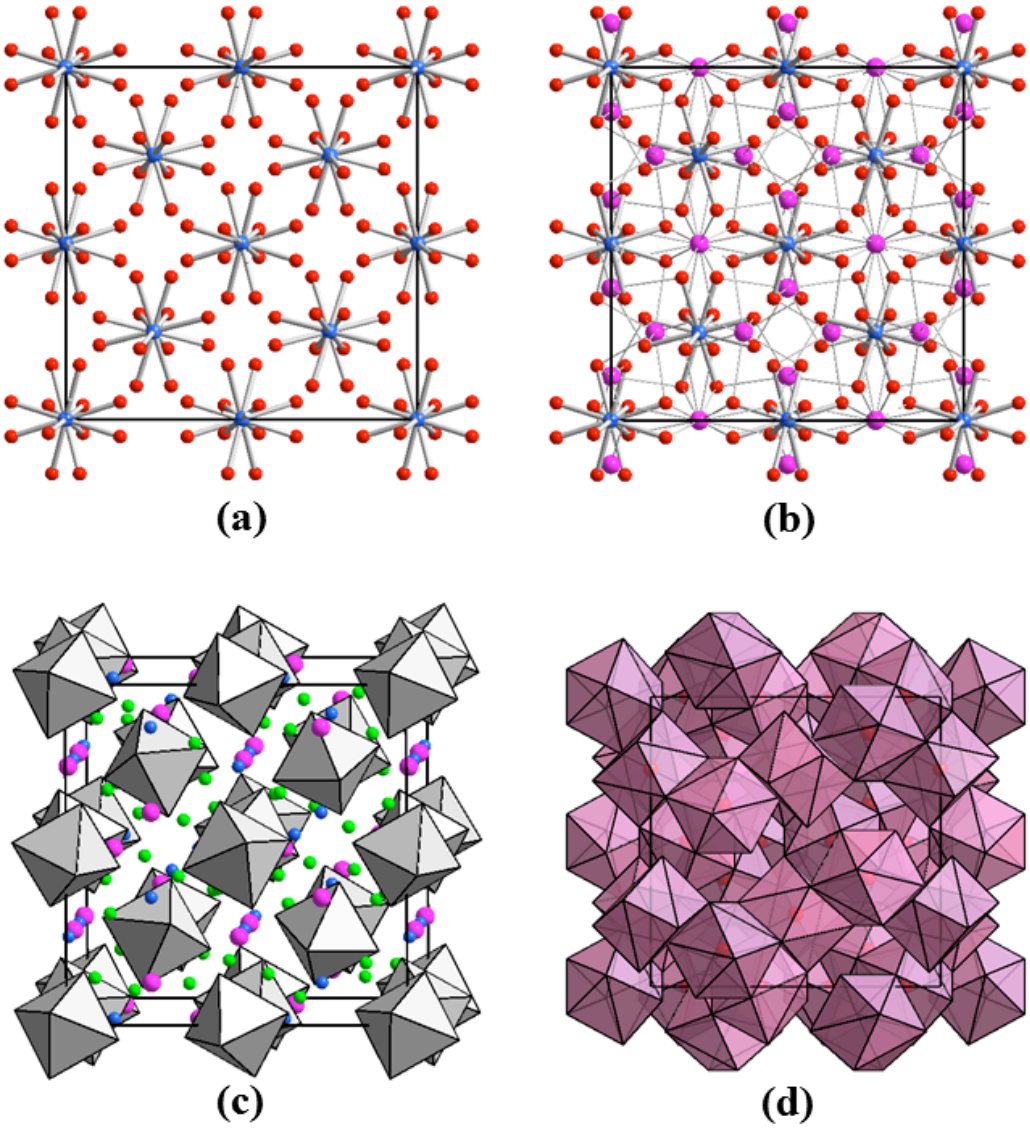

Figure 2. The garnet-type structure of $Li_{5+2x}La_3Ta_{2-x}Y_xO_{12}$. **(a)** Ta-O sublattice. Ta is shown in blue and oxygen in red. **(b)** Ta-O sublattice with La (purple) in spaces between TaO_6 units. **(c)** TaO_6 units shown by grey octahedra. La atoms are in purple, while Li1 (24d site) and Li2 (48g site) are shown as blue and green spheres, respectively. Li3 (96h site) is omitted for clarity. **(d)** The La-O sublattice showing LaO_8 polyhedra.

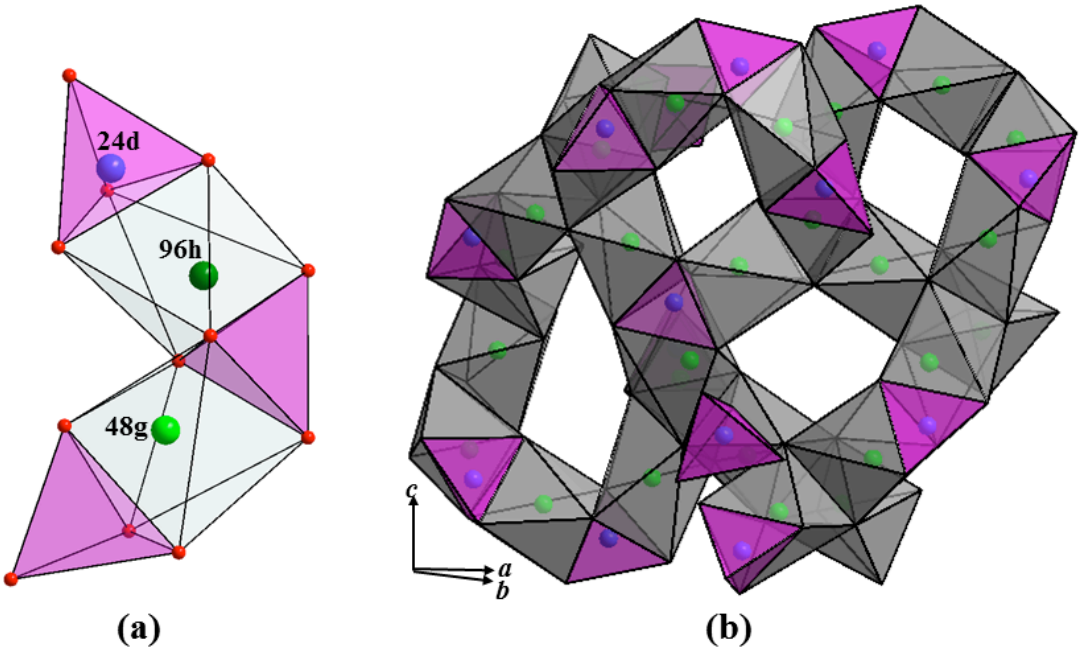

Figure 3. (a) The tetrahedral and octahedral arrangements of oxygens that accommodate the Li atoms. Oxygens are shown as small red spheres at the corners of polyhedra. The Li atoms at the centers of tetrahedra (24d site) and octahedra (48g site) are shown in blue and light green, respectively. The Li atom that is shifted from the center of the octahedron (96h site) is shown in dark green. **(b)** Three-dimensional connectivity of oxygen octahedra and tetrahedra, which can accommodate Li atoms, shown as blue and green spheres. In the actual structure, not all of the neighboring sites can be simultaneously occupied by Li and it is not possible for a Li atom to exist at an octahedral site if both tetrahedral sites adjacent to it are occupied.

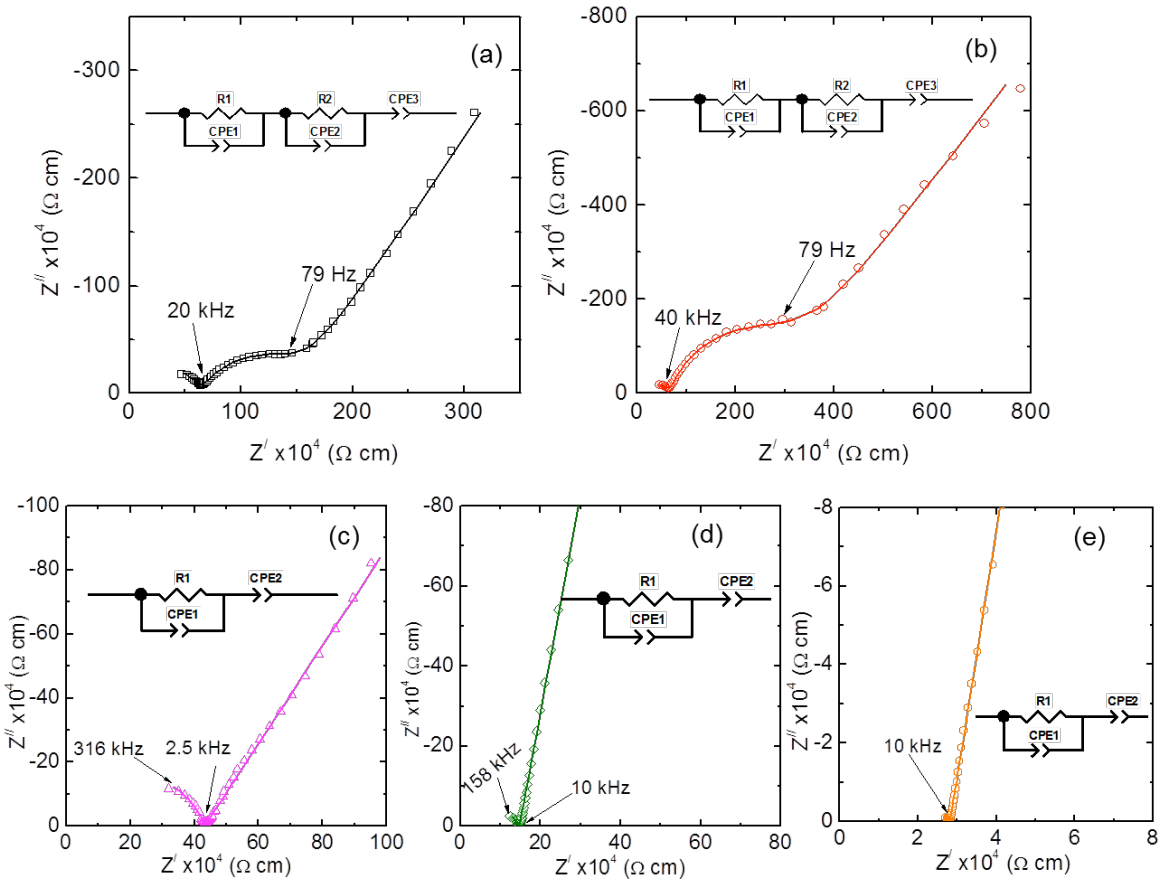

Figure 4. Typical AC impedance plots at 23 °C for $Li_{5+2x}La_3Ta_{2-x}Y_xO_{12}$ ($0.05 \leq x \leq 0.5$) (a) x = 0.05, (b) x = 0.10, (c) x = 0.20, (d) x = 0.25, and (e) x = 0.50. The open symbols represent the collected data and the solid lines represent the fitting. The inset figure indicates the equivalent circuits used for fitting analysis.

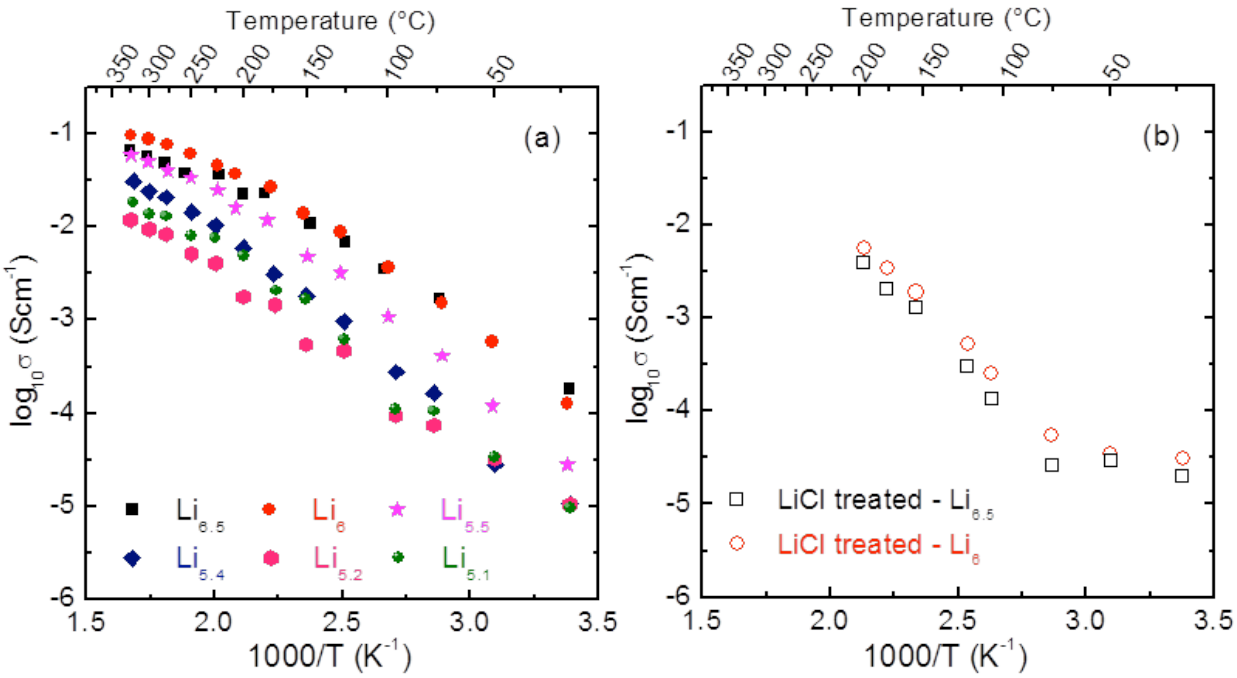

Figure 5. Arrhenius plots showing the conductivity variation against temperature of a) as-prepared $Li_{5+2x}La_3Ta_{2-x}Y_xO_{12}$ ($0.05 \leq x \leq 0.75$) and b) $Li_{5+2x}La_3Ta_{2-x}Y_xO_{12}$ ($x = 0.5$, and 0.75) after treatment with 1 M LiCl solution.

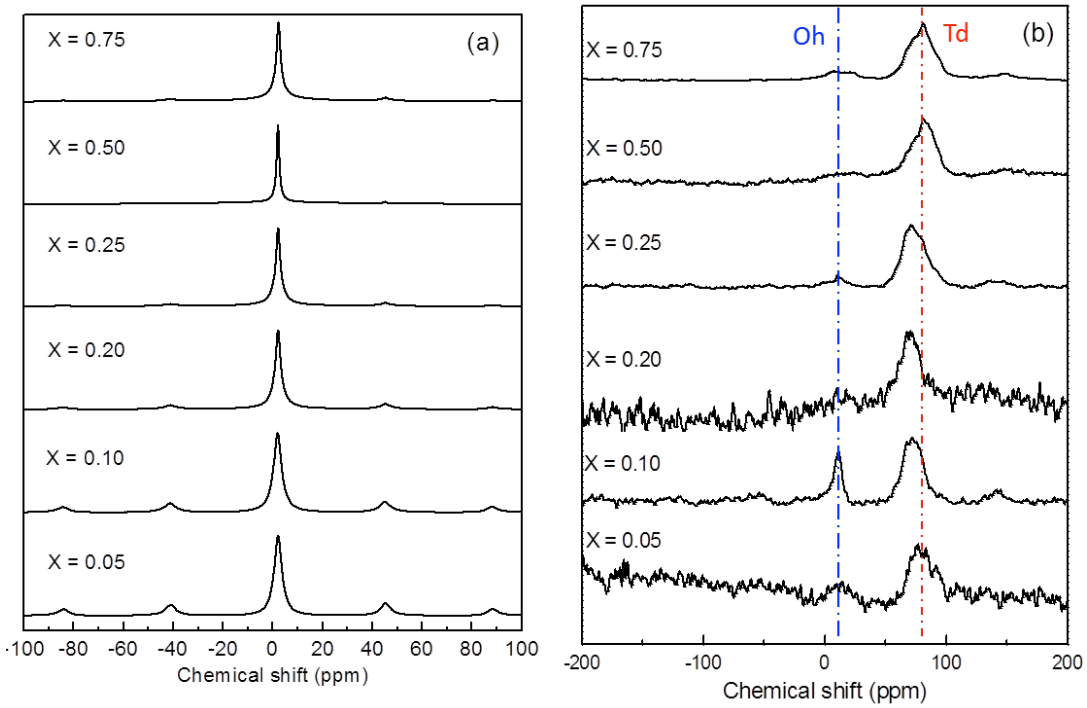

Figure 6. (a) ^{7}Li and (b) ^{27}Al MAS NMR of $Li_{5+2x}La_3Ta_{2-x}Y_xO_{12}$ ($0.05 \leq x \leq 0.75$). Chemical shift was measured against solid LiCl for Li MAS, and $Al(NO_3)_3$ for Al MAS NMR. A spinning frequency of 5 kHz was used.

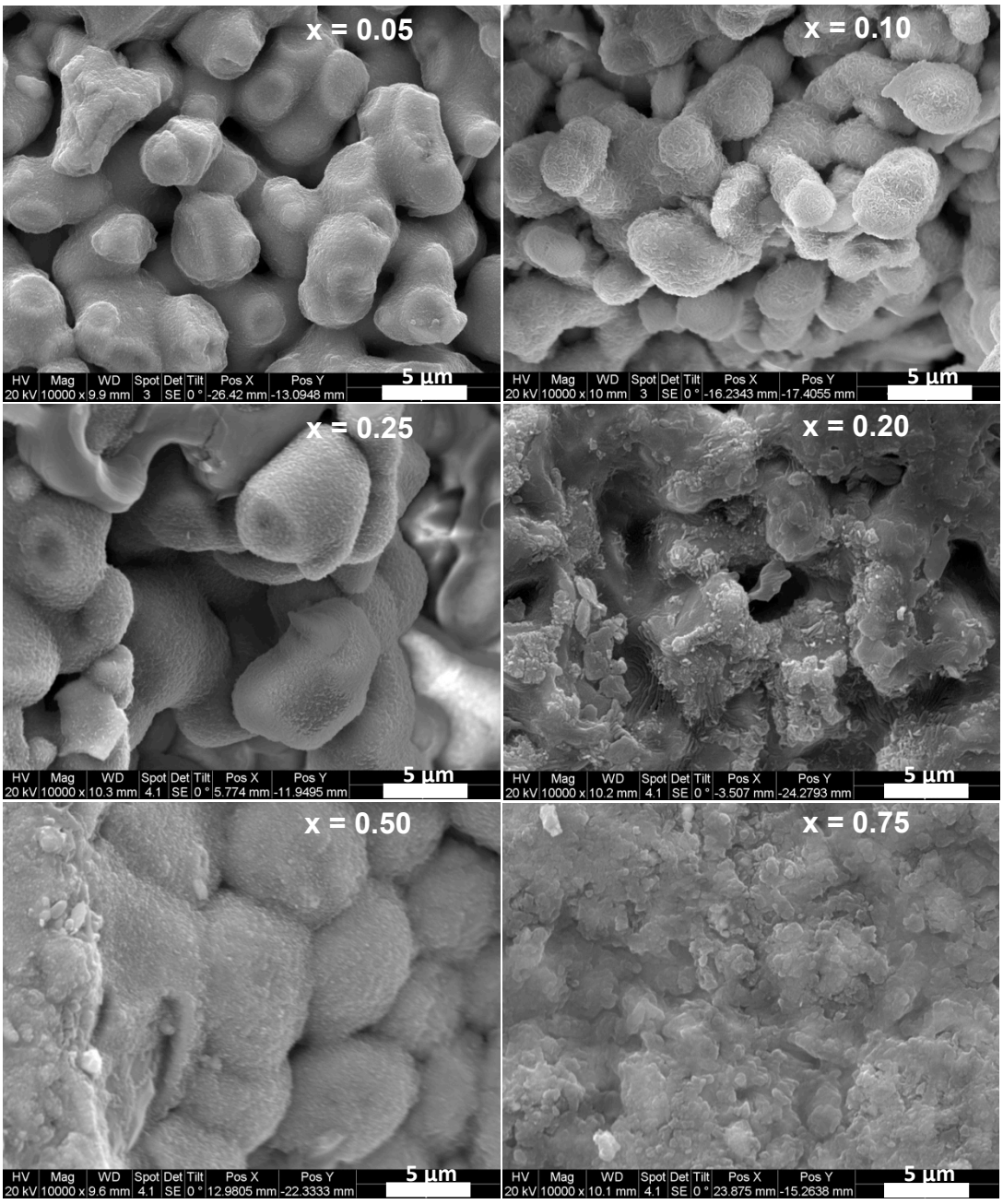

Figure 7. Morphological studies of $Li_{5+2x}La_3Ta_{2-x}Y_xO_{12}$ (x = 0.05–0.75) pellets using SEM microscopy.

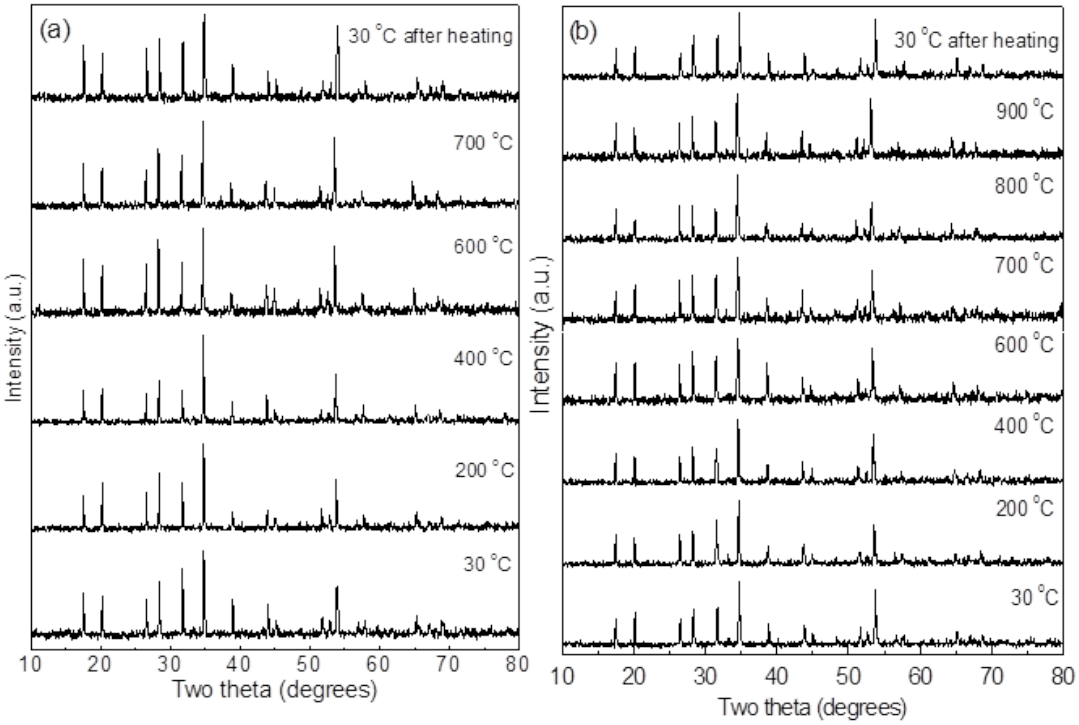

Figure 8. In situ PXRD of $Li_{5+2x}La_3Ta_{2-x}Y_xO_{12}$ (a) x = 0.25 and (b) x = 0.5 showing the thermal stability.

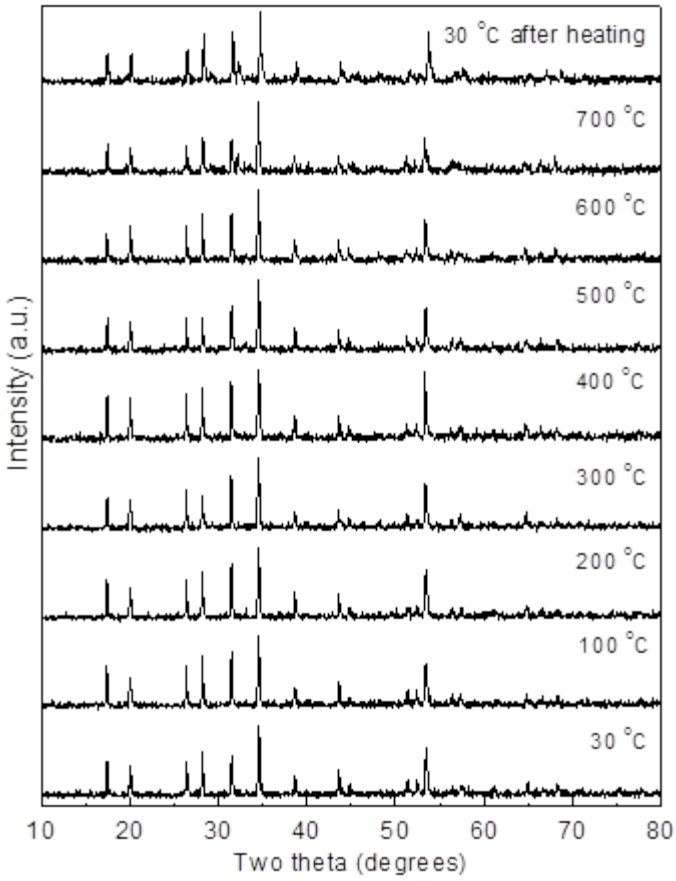

Figure 9. In situ PXRD patterns of water treated $Li_6La_3Ta_{1,5}Y_{0.5}O_{12}$ showing the structural stability.

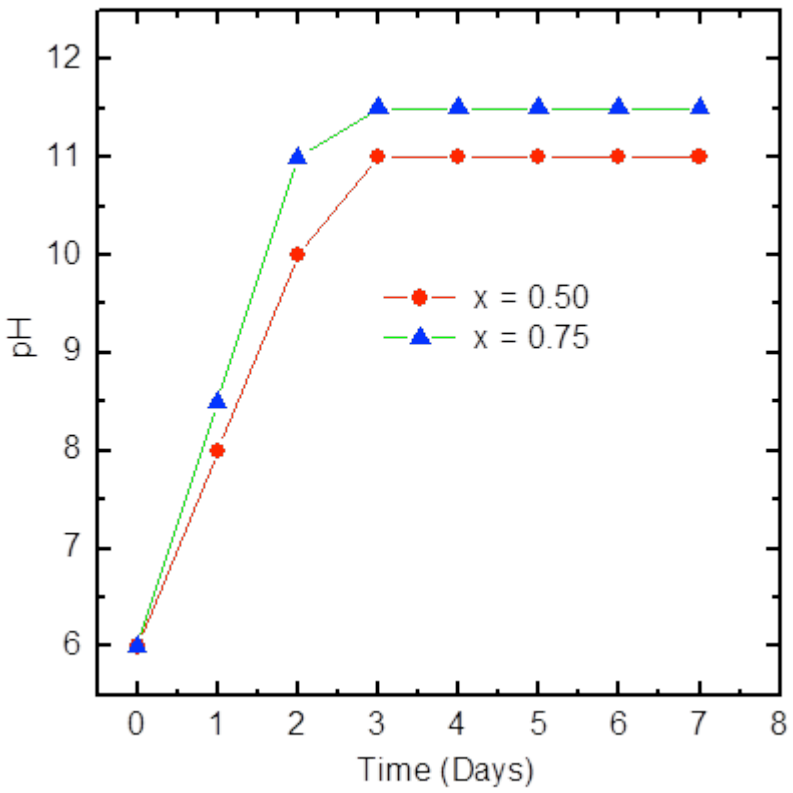

Figure 10. Changes in the pH during the treatment of $Li_{5+2x}La_3Ta_{2-x}Y_xO_{12}$ (x = 0.50 and 0.75) in 1 M LiCl solution.

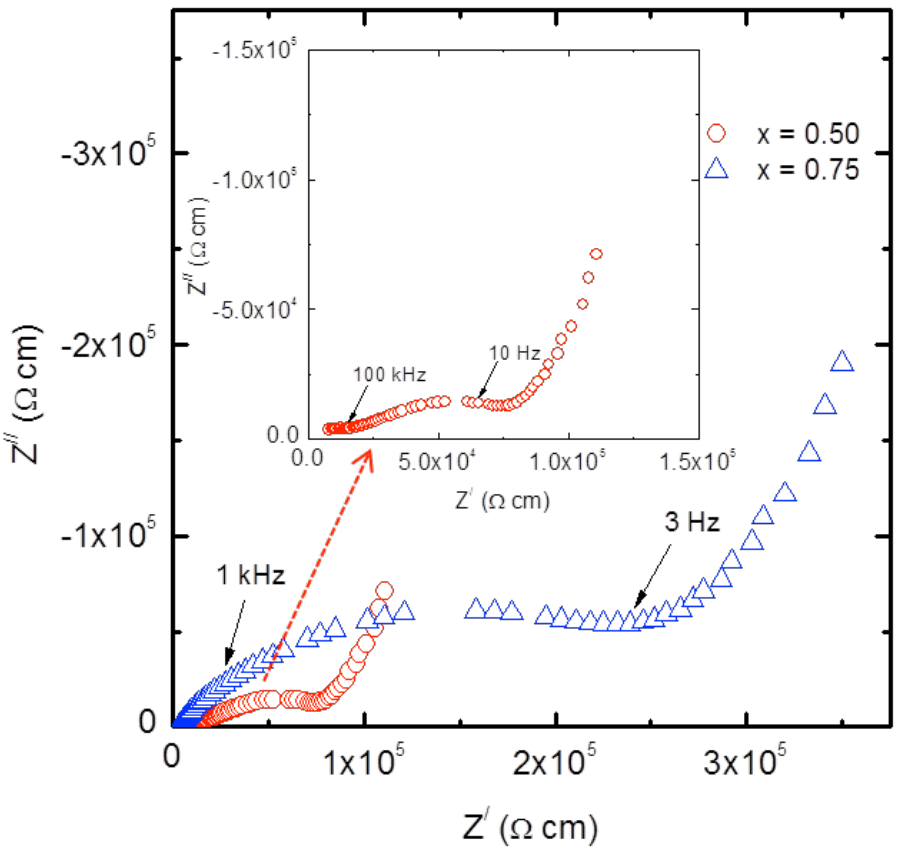

Figure 11. Impedance spectra of $Li_{5+2x}La_3Ta_{2-x}Y_xO_{12}$ (x = 0.50 and 0.75) after treatment with 1 M LiCl solution measured at 75 °C. The inset magnifies the data for x = 0.50 sample to show the small semi-circle at the high frequency side.

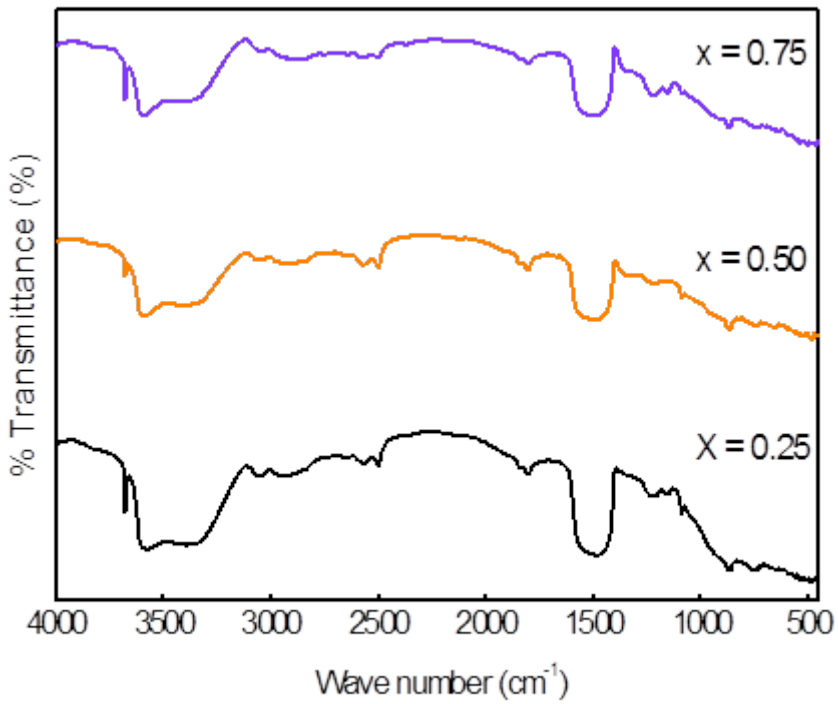

Figure 12. FTIR spectra of water-treated $Li_{5+2x}La_3Ta_{2-x}Y_xO_{12}$ (x = 0.25, 0.5 and 0.75).

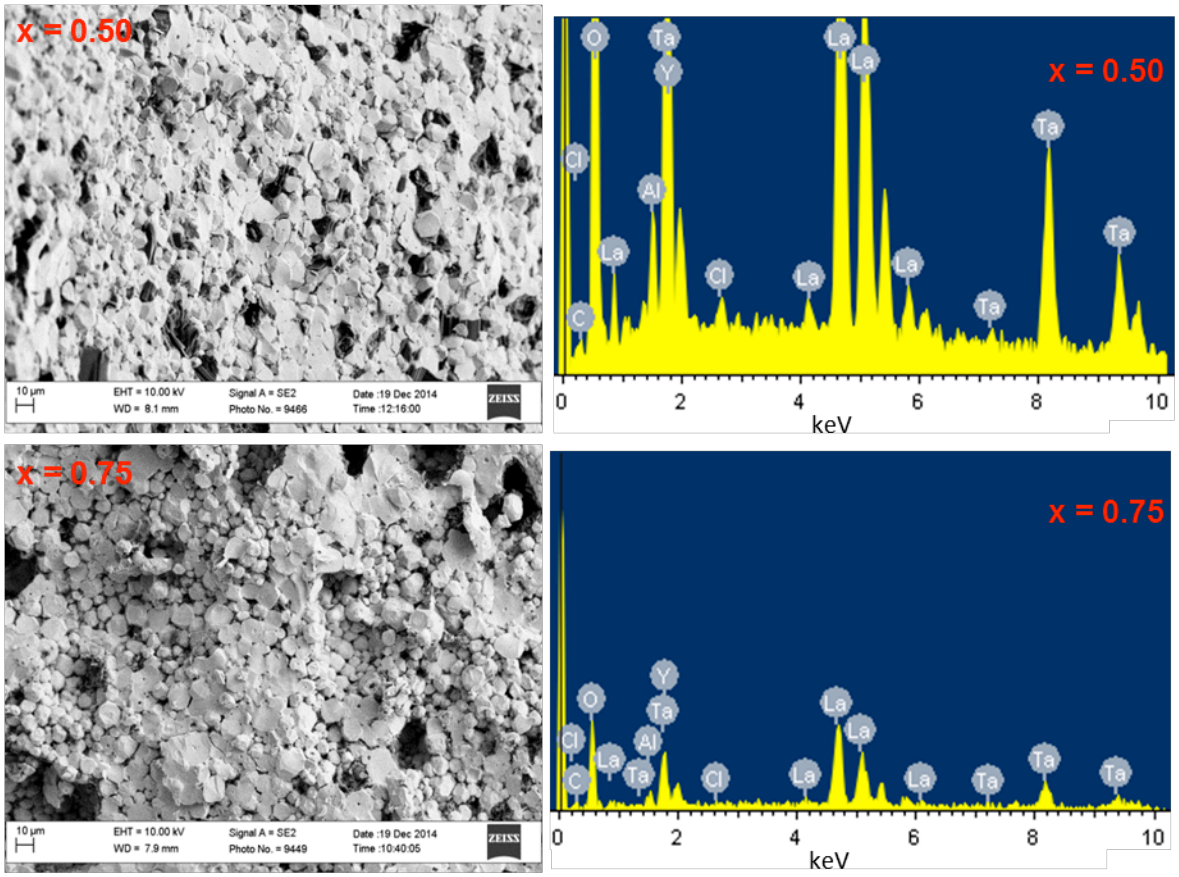

Figure 13. SEM images and EDX results for $Li_{5+2x}La_3Ta_{2-x}Y_xO_{12}$ (x = 0.5 and 0.75) after treatment with 1 M LiCl solution.

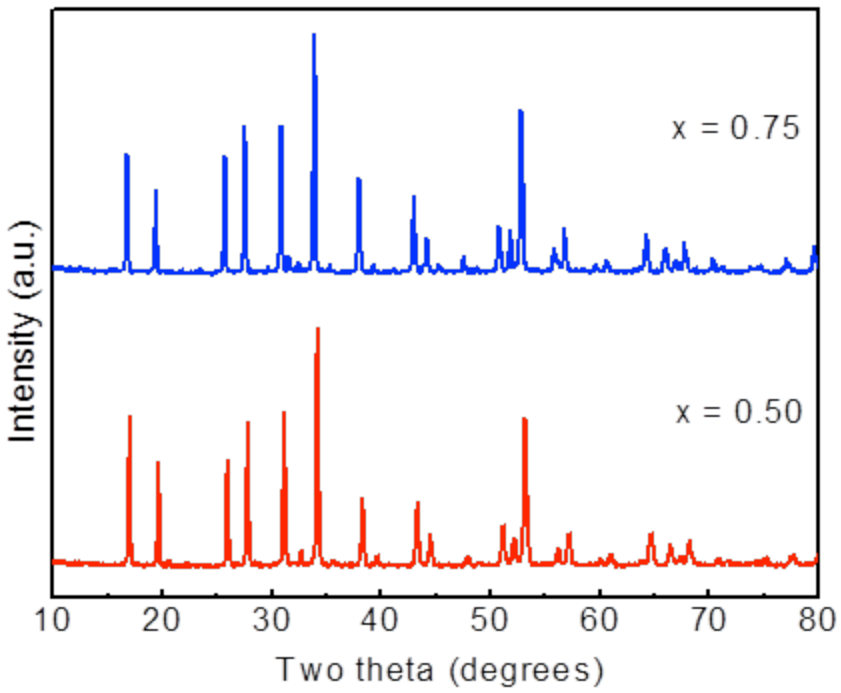

Figure 14. PXRD of $Li_{5+2x}La_3Ta_{2-x}Y_xO_{12}$ (x = 0.5 and 0.75) after reaction with 1 M LiCl solution.

REFERENCES

(1) Thangadurai, V.; Narayanan, S.; Pinzaru, D., *Chem. Soc. Rev.* **2014,** *43*, 4714-4727.

(2) Thangadurai, V.; Pinzaru, D.; Narayanan, S.; Baral, A. K., *J. Phys. Chem. Lett.* **2014**, 292-299.

(3) Shimonishi, Y.; Toda, A.; Zhang, T.; Hirano, A.; Imanishi, N.; Yamamoto, O.; Takeda, Y., *Solid State Ionics* **2011,** *183*, 48-53.

(4) Girishkumar, G.; McCloskey, B.; Luntz, A. C.; Swanson, S.; Wilcke, W., *J. Phys. Chem. Lett.* **2010**, 2193-2203.

(5) Ma, C.; Rangasamy, E.; Liang, C.; Sakamoto, J.; More, L. K.; Chi, M., *Angew. Chem. Int. Ed.* **2014,** *53*, 1-6.

(6) Thangadurai, V.; Kaack, H.; Weppner, W. J. F., *J. Am. Ceram. Soc.* **2003,** *86*, 437-440.

(7) Thangadurai, V.; Weppner, W., *Adv. Funct. Mater.* **2005,** *15*, 107-112.

(8) Thangadurai, V.; Weppner, W., *J. Am. Ceram. Soc.* **2005,** *88*, 411-418.

(9) Murugan, R.; Thangadurai, V.; Weppner, W., *Ionics* **2007,** *13*, 195-203.

(10) O'Callaghan, M. P.; Cussen, E. J., *Solid State Sciences* **2008,** *10*, 390-395.

(11) Xie, H.; Li, Y.; Han, J.; Dong, Y.; Paranthaman, M. P.; Wang, L.; Xu, M.; Gupta, A.; Bi, Z.; Bridges, C. A.; Nakanishi, M.; Sokolov, A. P.; Goodenough, J. B., *J. Electrochem. Soc.* **2012,** *159*, A1148-A1151.

(12) Murugan, R.; Thangadurai, V.; Weppner, W., *Angew. Chem. Int. Ed. Engl.* **2007,** *46*, 7778-81.

(13) Awaka, J.; Kijima, N.; Hayakawa, H.; Akimoto, J., *J. Solid State Chem.* **2009,** *182*, 2046-2052.

(14) Geiger, C. A.; Alekseev, E.; Lazic, B.; Fisch, M.; Armbruster, T.; Langner, R.; Fechtelkord, M.; Kim, N.; Pettke, T.; Weppner, W., *Inorg. Chem.* **2011,** *50*, 1089-97.

(15) Buschmann, H.; Dolle, J.; Berendts, S.; Kuhn, A.; Bottke, P.; Wilkening, M.; Heitjans, P.; Senyshyn, A.; Ehrenberg, H.; Lotnyk, A.; Duppel, V.; Kienle, L.; Janek, J., *Phys. Chem. Chem. Phys.* **2011,** *13*, 19378-92.

(16) Rangasamy, E.; Wolfenstine, J.; Sakamoto, J., *Solid State Ionics* **2012,** *206*, 28-32.

(17) Lee, J.-M.; Kim, T.; Baek, S.-W.; Aihara, Y.; Park, Y.; Kim, Y.-I.; Doo, S.-G., *Solid State Ionics* **2014,** *258*, 13-17.

(18) Wolfenstine, J.; Sakamoto, J.; Allen, J. L., *J. Mater. Sci.* **2012,** *47*, 4428-4431.

(19) Buschmann, H.; Berendts, S.; Mogwitz, B.; Janek, J., *J. Power Sources* **2012,** *206*, 236-244.

(20) Thompson, T.; Wolfenstine, J.; Allen, J. L.; Johannes, M.; Huq, A.; Davida, I. N.; Sakamoto, J., *J. Mater. Chem. A,* **2014,** *2*, 13431-13436.

(21) Li, Y.; Han, J.-T.; Wang, C.-A.; Vogel, S. C.; Xie, H.; Xu, M.; Goodenough, J. B., *J. Power Sources* **2012,** *209*, 278-281.

(22) Murugan, R.; Ramakumar, S.; Janani, N., *Electrochem. Comm.* **2011,** *13*, 1373-1375.

(23) Ohta, S.; Kobayashi, T.; Asaoka, T., *J. Power Sources* **2011,** *196*, 3342-3345.

(24) Narayanan, S.; Ramezanipour, F.; Thangadurai, V., *J. Phys. Chem. C* **2012,** *116*, 20154-20162.

(25) Baral, A. K.; Narayanan, S.; Ramezanipour, F.; Thangadurai, V., *Phys. Chem. Chem. Phys.* **2014,** *16*, 11356-65.

(26) Larson, C. A.; Von Dreele, B. R., *Los Alamos National Laboratory Report LAUR* **1994**, 86−748.

(27) Toby, B. H., *J. Appl. Cryst.* **2001,** *34*, 210-213.

(28) Shannon, R. D., *Acta Cryst.* **1976,** *A 32*, 751-767.

(29) Muller, O.; Roy.R., *The Major Ternary Structural Families. Crystal Chemistry of Non-Metallic Materials*. **1975,** *10*, 177-178.

(30) Cussen, E. J., *Chem. Comm.* **2006**, 412-413.

(31) O'Callaghan, M. P.; Cussen, E. J., *Chem. Comm.* **2007**, 2048-2050.

(32) Cussen, E. J., *J. Mater. Chem.* **2010,** *20*, 5167.

(33) Narayanan, S.; Thangadurai, V., *J. Power Sources* **2011,** *196*, 8085-8090.

(34) Irvine, J. T. S.; Sinclair, D. C.; West, A. R., *Adv. Mater.* **1990,** *2*, 132-138.

(35) Dumon, A.; Huang, M.; Shen, Y.; Nan, C.-W., *Solid State Ionics* **2013,** *243*, 36-41.

(36) Narayanan, S.; Epp, V.; Wilkening, M.; Thangadurai, V., *RSC Advances* **2012,** *2*, 2553.

(37) Rettenwander, D.; Langer, J.; Schmidt, W.; Arrer, C.; Harris, K. J.; Terskikh, V.; Goward, G. R.; Wilkening, M.; Amthauer, G., *Chem. Mater.* **2015,** *27*, 3135-3142.

(38) Gore, M. C.; White, O. J.; Wachsman, D. E.; Thangadurai, V., *J. Mater. Chem. A* **2014,** *2*, 2363–2373.

(39) Handal, H. T.; Thangadurai, V., *J. Power Sources* **2013,** *243*, 458-471.

(40) Truong, L.; Thangadurai, V., *Chem. Mater.* **2011,** *23*, 3970-3977.

(41) Liu, C.; Rui, K.; Shen, C.; Badding, M. E.; Zhang, G.; Wen, Z., *J. Power Sources* **2015,** *282*, 286-293.

Table of Contents

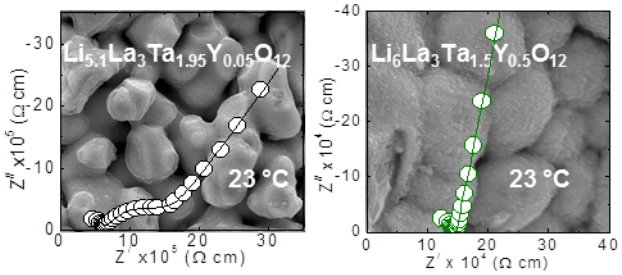

Porosity, chemical stability in aqueous solution, and Li-ion conductivity of a series of garnet-type $Li_{5+2x}La_3Ta_{2-x}Y_xO_{12}$ were studied as a function of Y and Li-doping. An increase in Li conductivity and decrease in porosity were observed as Y and Li contents increased. The observation of high structural stability upon treatment in aqueous LiCl makes these materials interesting candidates for potential application as protective layers for lithium electrodes in aqueous lithium batteries.